Applied Thermal Engineering 280 (2025) 128253

Contents lists available at ScienceDirect

Applied Thermal Engineering

journal homepage: www.elsevier.com/locate/apthermeng

Research Paper

Experimental investigation of heat transfer and pressure losses across additively manufactured Body Centered Cubic arrays: effects of cell shape and array arrangement

Emanuele Vaglio, Federico Scalzo, Nicolò Scussolin, Luca Casarsa *

Polytechnic Department of Engineering and Architecture, University of Udine, Via delle Scienze 206, Udine, 33100, Italy

ARTICLE INFO

Keywords:
Laser powder bed fusion
Heat sinks
Body centred cubic arrays
Heat transfer
Pressure losses

ABSTRACT

This study experimentally investigates the thermo-hydraulic performance of heat sinks featuring Body-Centered Cubic (BCC) lattices produced from AlSi10Mg via Laser Powder Bed Fusion. The objective is to assess the influence of key design parameters, such as truss inclination, lattice layout, and streamwise pitch on heat transfer and pressure drop characteristics. To this aim, the samples geometrical conformity and surface roughness were first characterized using optical and non-destructive methods, confirming good dimensional accuracy, although occasional surface defects caused by thermal distortion or dross formation were observed. Subsequently, tests were conducted on a dedicated test rig over Reynolds numbers ranging from 5000 to 27500, collecting pressure drop data under isothermal conditions and heat transfer data under uniform heat flux boundary conditions. The results showed that reducing the streamwise pitch improves thermal performance but also increases flow resistance. Conversely, staggered configurations reduce friction losses at the expenses of some heat transfer efficiency. Variations in truss inclination had instead minimal impact. The introduction of a modified hydraulic diameter quantifying the unit cell density, and the streamwise pitch parameter enabled a novel normalization method that successfully collapsed the performance data across all configurations. Finally, by evaluating the Thermal Performance Factor for each dataset, the study identified the optimal trade-off between friction losses and thermal performances among all tested geometries.

1. Introduction

The growing need for compact, lightweight, and energy-efficient thermal management systems across high-performance industries such as aerospace [1], automotive [2], electronics [3], and renewable energy [4] has spurred significant advances in heat exchanger design. Their performance directly affects efficiency, reliability, and operational safety of the systems they support. However, traditional manufacturing techniques—such as milling, welding, brazing, and extrusion—limit the design and performance potential of HXs. These subtractive methods generate material waste and require complex assemblies, adding weight and increasing the risk of leaks at joints.

Recent breakthroughs in additive manufacturing (AM), particularly metal 3D printing, offer a transformative shift in heat exchangers design and production. By constructing components layer by layer from digital models, AM minimizes material waste and enables the fabrication of monolithic structures with highly intricate geometries previously unattainable through conventional methods [5]. This design flexibility enables conformal flow paths, multiscale features, and increased surface area, all of which enhance heat transfer efficiency and reduced pressure losses [6]. These capabilities are further amplified by the integration of computational design tools and optimization algorithms [7–9], which enable systematic tailoring of internal topologies to optimize thermo-hydraulic performance.

To enhance thermal effectiveness, several strategies are widely adopted in modern heat exchangers designs. These include surface texturing, microchannel integration, turbulence promoters, cellular materials, and more advanced heat transfer mechanisms such as jet impingement and heat pipes [2]. Among these, cellular materials and turbulence promoters have garnered particular interest due to the geometric complexity they can assume when manufactured via AM. This stimulated extensive research focused on engineered structures like triply periodic minimal surfaces (TPMS) and lattice architectures, which demonstrate significant potential for enhancing temperature uniformity, promoting turbulence, and optimizing flow distribution [10–12].

* Corresponding author.
E-mail address: luca.casarsa@uniud.it (L. Casarsa).

https://doi.org/10.1016/j.applthermaleng.2025.128253
Received 20 June 2025; Received in revised form 4 August 2025; Accepted 5 September 2025
Available online 6 September 2025

Nomenclature

Latin symbols

A_c	flow cross-section area [m^2]
A_r	reference surface area for heat transfer [m^2]
A_w	wetted surface area [m^2]
c_p	specific heat capacity [J/(kg K)]
d_x	BCC dimension in streamwise direction [m]
d_y	BCC dimension in crosswise direction [m]
D_{BCC}	hydraulic diameter of the heat exchanger [m]
D_h	hydraulic diameter [m]
E	supplied voltage [V]
f	friction factor
f_0	friction factor of the smooth channel
f_n	modified friction factor
h	Convective heat transfer coefficient [W/m^2 K]
H	channel height [m]
I	supplied current intensity [A]
k	thermal conductivity [W/(Km)]
$L_{\Delta p}$	distance between pressure taps [m]
$\dot{m}$	air flow rate [kg/s]
Nu	Nusselt number
Nu_0	Nusselt number of the smooth channel
Nu_n	modified Nusselt number
P	wet perimeter of the flow area [m]
Δp	pressure drop [Pa]
Q_{air}	heat rate received by air [W]
Q_{el}	input heat power [W]
R	overall thermal resistance [K/W]
Ra	roughness average [μm]
Re	channel Reynolds number
Re^*	modified channel Reynolds number
S_x	streamwise BCC spacing [m]
S_y	spanwise BCC spacing [m]
T_{Al}	internal temperature of the instrumented aluminum block [°C]
T_{IN}	inlet air temperature [°C]
T_{OUT}	outlet air temperature [°C]
$T_{OUT,c}$	air temperature at the throat section [°C]
T_w	internal channel surface temperature [°C]
ΔT_{ml}	log mean temperature difference [°C]
U_b	bulk velocity [m/s]
U_{IN}	bulk velocity at the section inlet [m/s]
$U_{OUT,c}$	bulk velocity at the outlet throat section [m/s]
V_w	enclosed wetted volume [m^3]
Wa	waviness average [μm]
X, Y, Z	channel reference system: streamwise, spanwise and crosswise directions

Greek symbols

α	thermal diffusivity
ε	mean height of roughness [μm]
λ_c	cut-off wavelength [mm]
μ	dynamic viscosity [Pa s]
ρ	density [kg/m^3]

Acronyms

AM	Additive Manufacturing
BCC	Body-Centered Cubic
FEA	Finte Element Anlysis
LPBF	Laser Powder Bed Fusion
MDF	Medium-Density Fibreboard
SEM	Scanning Electron Microscope
TC	Thermocouple
TPF	Thermal Performance Factor
TPMS	Triply Periodic Minimal Surfaces

Several numerical and experimental studies have demonstrated the thermohydraulic benefits of TPMS-based and lattice-structured heat exchangers. Song et al. [13], Catchpole-Smith et al. [14] and Vaglio et al. [15] investigated gyroid and other TPMS geometries, highlighting how unit cell size, porosity ratio, and volume fraction significantly influence heat transfer and thermal conductivity. Tang et al. [16] further enhanced a TPMS structure by integrating pin fins, identifying mechanisms such as longitudinal vortex generation and increased surface area as contributors to thermal improvement. Gao et al. [17] explored cell size gradients in AM copper structures, showing that smaller cells enhanced heat transfer but increased pressure drop, revealing a performance trade-off between effectiveness and pressure penalty. Huang et al. [18] and Park et al. [19] extended these insights by quantifying thermal conductivity in BCC lattices and analyzing the influence of structural parameters such as strut diameter and inclination angle.

Lattice-frame materials combine porosity, a high surface area-to-volume ratio, and structural stability [20], making them well-suited for aerospace applications. Narkhede et al. [21] evaluated octet lattice heat sinks fabricated from AlSi10Mg, finding that reduced porosity and smaller unit cells enhanced thermal dissipation but increased pressure loss. Lorenzon et al. [22] investigated the thermal and fluid dynamic performance of BCC arrays with circular cross sections, showing that an increase in strut diameter can intensify both heat transfer and pressure losses, thereby resulting in comparable overall performance, and that normalization by the BCC hydraulic diameter enables the formulation of reliable predictive correlations. Wong et al. [23] compared conventional and innovative fin geometries, revealing that staggered arrays of elliptical cross section fins offered the best balance between heat transfer and pressure drop, while complex lattice designs sometimes underperformed due to poor fluid interaction. Lorenzon et al. [24] confirmed the superior performance of the elliptical cross section in BCC arrays by comparing its thermal and fluid dynamic behavior against circular, drop, and cam cross sections. They found that tapered profiles lower pressure losses, boost Nusselt numbers, and provide a Thermal Performance Factor (TPF) above one, even at high Reynolds numbers. Elliptical trusses showed the best overall performance.

A particularly notable contribution is that of Kemerli et al. [25], who conducted a numerical analysis of conjugate forced convection in a sandwich panel heat exchanger featuring a Kagome truss core. Their study examined the influence of Reynolds number, strut length, and diameter under both constant heat flux and constant temperature boundary conditions. Results indicated that shorter strut lengths significantly improved heat transfer due to induced complex flow structures and vortex formation. While larger diameters slightly increased thermal performance, their effect diminished at shorter lengths. Importantly, Kemerli et al. emphasized that unit cell geometry plays a critical role in defining the overall thermal and hydraulic response, and that heat transfer can be improved at a fixed pumping power by selecting appropriate geometric parameters. These findings underscore the importance of geometrically optimized truss architectures in designing next-generation heat exchangers.

Complementary to cellular structures, turbulence promoters have also proven effective in enhancing convective heat transfer. Narato et al. [26] demonstrated how angled cylindrical pins generate counter-rotating vortices, improving thermal performance with reduced pressure losses. Similarly, Maji et al. [27] and Zhao et al. [28] analyzed perforated and angled pin fins, emphasizing how optimized shapes and layouts can improve heat dissipation and energy efficiency. Lorenzon

et al. [29] investigated the thermal and hydraulic performance of pin–fin arrays in annular channels, optimizing the pin geometry while accounting for manufacturability constraints. Sertkaya et al. [30] further evaluated natural convection and radiation effects in pin fin configurations, while Xu et al. [31] explored X-shaped vortex generators in fin-tube heat exchangers, employing artificial intelligence-driven optimization to significantly boost thermal performance. Notably, Vaglio et al. [15] recently showed that these types of structures still outperform the most advanced architectures currently attracting attention in both academia and industry.

Despite extensive recent research, key gaps remain in the current literature. Studies often lack standardized metrics for comparing thermal and hydraulic performance, and inconsistencies in defining geometric parameters impede the development of generalized design guidelines. Furthermore, many investigations rely exclusively on numerical simulations without accounting for manufacturability constraints or the actual physical properties of AM materials. Detailed characterization of surface morphology, roughness, dimensional accuracy, and thermal conductivity is frequently omitted, compromising the replicability and applicability of proposed solutions. A summary of the most relevant recent works investigating the thermo-fluid dynamic behavior of engineered materials and pin fin arrays is provided in Table 1.

To address these gaps, future research should focus on relatively simple yet representative geometries tested under standardized conditions to produce reliable datasets and performance correlations. This strategy will enable more robust, data-driven development of next-generation heat exchangers.

Building upon previous studies that sequentially optimized the truss size and cross-sectional shape of Body-Centered Cubic lattice structures [22,24], this work systematically investigates the effects of higher-order geometric parameters, namely truss aperture angle, lattice spatial configuration, and streamwise pitch variation, on the thermal and hydraulic performance of qualified BCC lattice structures fabricated from AlSi10Mg using Laser Powder Bed Fusion. By so doing, fundamental dimensionless groups for the normalization of the observed phenomena were successfully derived, and the parameters governing performance were identified, thereby providing valuable insights and a practical framework for the predictive design and optimization of advanced lattice-based thermal management solutions.

Table 1
Overview of key studies examining the properties of advanced structures for thermal management.

Ref.	Structure type	Production Process	Analysis method
[13]	TPMS (Gyroid)	–	FEA
[14]	TPMS (Gyroid, Diamond, Schwarz)	LPBF (Hastelloy-X and Ti6Al4V)	FEA and thermal conductivity
[15]	TPMS (Gyroid), Lattice (BCC and Octahedral), Pin Fins	LPBF (316L SS)	Experimental investigation on heat transfer and pressure drop
[16]	TPMS (Gyroid) + Pin Fins	LPBF (AlSi10Mg)	FEA and experimental termofluidynamic investigation
[17]	TPMS (Gradient Cell Size)	LPBF (Pure Copper)	FEA, wall thickness and surface roughness (RH-2000 optical microscope) and experimental termofluidynamic investigation
[18]	BCC Lattice (Gradient Porosity)	LPBF (316L SS)	FEA, truss diameter (SEM) and thermal conductivity
[19]	BCC Lattice	LPBF (AlSi7Mg)	FEA and experimental termofluidynamic investigation
[20]	Lattice-Frame Material (Tetrahedral)	Polyjet and Binderjet (Fullcure 720 and 420 stainless steel and bronze)	FEA and experimental termofluidynamic investigation
[21]	Octet Lattice	–	FEA
[22]	BCC Lattice	LPBF (AlSi10Mg)	Experimental investigation on heat transfer and pressure drop
[23]	Pin Fins, Lattice, Fins (Rounded/Elliptic)	LPBF (Al6061)	Convective heat transfer and pressure losses investigation
[24]	BCC Lattice (Rounded/Elliptic/Drop/Cam)	LPBF (AlSi10Mg)	Experimental investigation on heat transfer and pressure drop
[25]	Kagome Truss	–	FEA
[26]	Inclined Cylindrical Pin Fins	–	FEA, flow and heat transfer characteristics investigation
[27]	Perforated Pin Fins	–	FEA, validation with existing numerical and experimental work
[28]	Square Micro Pin Fins	–	FEA (optimization of shape and layout)
[29]	Pin Fins	LPBF (316L SS)	Experimental investigation on heat transfer and pressure drop
[30]	Pin Fins and Plates	Al6011	Experimental investigation on natural convection heat transfer
[31]	Fin-Tube + X-shaped Vortex Gens	–	FEA, experimental termofluidynamic investigation and ANN optimization

2. Experimental methods

2.1. Investigated geometries

The geometries examined in this study are shown in Figs. 1 and 2. They are all derived from geometry A, which was selected from a previous study [24] as the best-performing among similar geometries that differ only in the shape of the BCC truss cross-section. In this investigation, the focus is on evaluating how the BCC truss aperture angle (affecting shape), the BCC matrix arrangement, and the pitch variation in the streamwise direction (S_x in Fig. 1) influence aero-thermal behavior. The pitch in the crosswise direction, S_y, is not considered in this study and will be addressed in future work.

The external dimensions of all specimens were kept constant (see Fig. 2) and consistent with previous studies [22,24]. Six geometries were defined, allowing a comparative analysis to isolate the effects of individual geometric parameters on aero-thermal performance. The initial geometry, designated as A, features an S_x equal to twice the length of the BCC unit in the same direction ($S_x = 28$ mm, $d_x = 14$ mm; see Table 2). From this configuration, the geometry labelled AP was derived by reducing S_x to 24 mm, corresponding to twice the average cell size in the x and y directions. A second variant, designated AS, is geometrically identical to the original but features a staggered placement of the unit cells in the y direction by half a pitch.

The geometries denoted B (and any suffixes) described below are all characterized by a variation in the shape of the unit cell. In particular, the angle formed by the axis of the rods with the confinement planes changes from 30° in geometry A to 45° in geometry B (see Fig. 2). This also alters the unit cell footprint, which becomes square (10 × 10 mm) instead of rectangular.

Geometry B exhibits cell positioning that is analogous to geometry A, and the cross-comparison of their results will therefore highlight only the effect of the BCC shape.

Starting from this geometry, and following the same criteria adopted to generate the geometries derived from A, pitch and relative row positioning variations were introduced. The following variations were thus obtained:

- BP: with respect to B, a reduction in pitch from 28 mm to 20 mm, which is twice the average of the BCC dimensions;

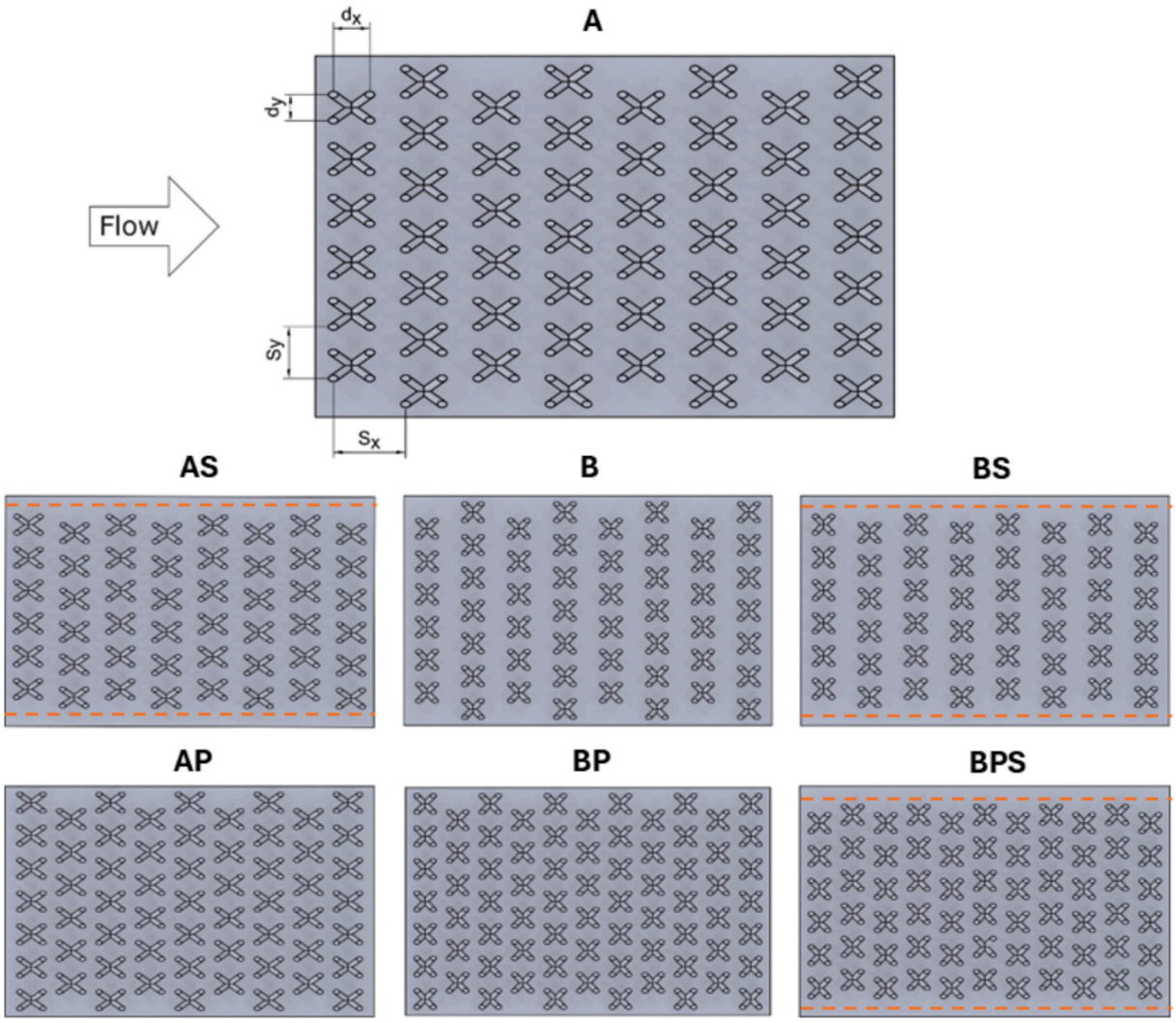

Fig. 1. Schematic view of the geometries selected for the investigation, red dashed lines indicate the actual position of the confining walls for *-mod geometries.

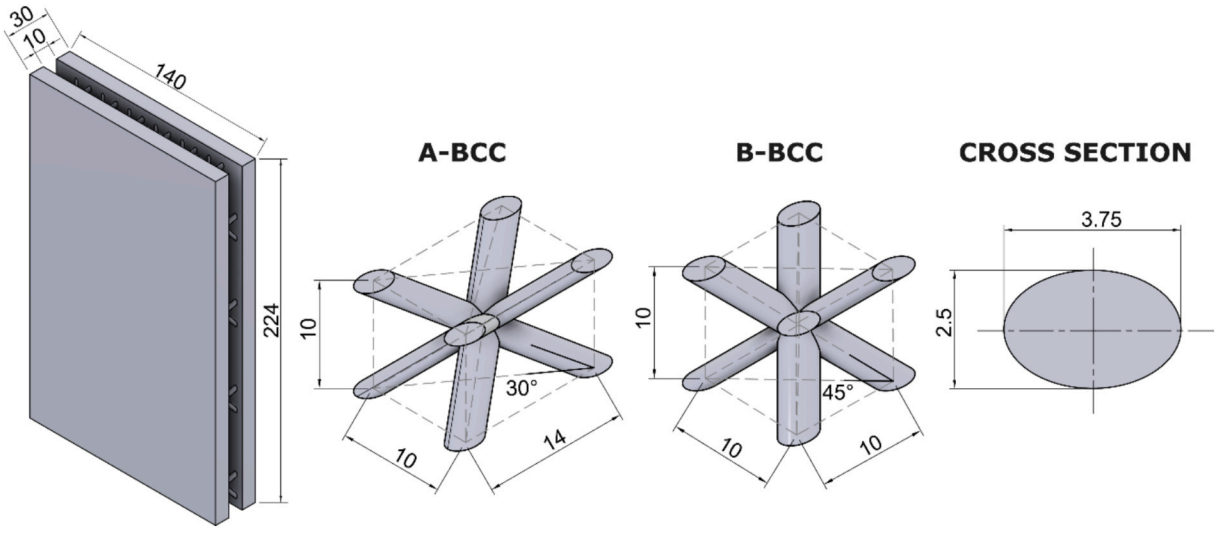

Fig. 2. Test section external dimensions (left), geometrical details of the BCC unitary cells (centre), and shape and dimension of the BCC truss cross section (right).

- BS: with respect to B, positioning in y direction staggered by half a pitch, resulting in a geometry identical to AS, except for the unit cell shape;
- BPS: compared to BS, a reduction in pitch to 20 mm (identical to the reduction applied to BP).

Table 2
Geometrical details of the investigated geometries.

Geometry	# of BCC	# of BCC rows	BCC Cell dimensions [mm]		Pitch [mm]		D_h [mm]	D_{BCC} [mm]
			d_x	d_y	S_x	S_y		
A	52	8	14	10	28	20	18.67	13.19
AP	59	9	14	10	24	20	18.67	12.68
AS	48	8	14	10	28	20	18.67	13.53
AS-mod	48	8	14	10	28	20	18.52	13.00
B	52	8	10	10	28	20	18.67	13.61
BP	72	11	10	10	20	20	18.67	12.25
BS	48	8	10	10	28	20	18.67	13.91
BS-mod	48	8	10	10	28	20	18.52	13.40
BPS	66	11	10	10	20	20	18.67	12.63
BPS-mod	66	11	10	10	20	20	18.52	12.07

As illustrated in Fig. 1 and Table 2, changes in pitch and matrix arrangement inevitably lead to variations in the number of rows, the number of elements per row and, consequently, the total number of unit elements constituting the heat exchanger, while the external dimensions remain constant. These variations naturally affect performance and will be accounted for in the subsequent data analysis through appropriate normalization.

Moreover, configurations with half-pitch staggered rows (AS, BS, and BPS) feature rows composed of six cells—rather than alternating between six and seven elements as in other configurations. This results in a larger gap between the lateral confinement wall and the first or last element of a row, potentially allowing for lateral bypass flow, which can impact the performance of the heat exchanger. Due to the complete lack of optical access inside the Aluminium test specimen, it was not possible to perform flow measurements or simple flow visualization to verify the existence and eventually quantify the by-pass flow. Therefore, to investigate this effect, geometries AS, BS, and BPS were modified by adding plexiglass side buffers made from a non-conductive material, similar to the outer side walls used throughout, to restore the minimum distance between a cell and the side wall to 5 mm, consistent with other geometries. The position of these lateral buffers is indicated by red dashed lines in Fig. 1. This modification reduces the crosswise dimension of the test section (from 140 mm to 125 mm) and decreases the inlet cross section area A_c, its perimeter P, and the hydraulic diameter D_h (from 18.67 mm to 18.52 mm), resulting in the modified geometries: AS-mod, BS-mod, and BPS-mod.

The specimens used in this study were produced using a Concept Laser M2 Cusing machine operating in an inert atmosphere consisting of 99.8 % argon. The AlSi10Mg alloy powder (see Table 3) exhibited a spherical morphology and a particle size distribution ranging from 23.2 μm (10th percentile) to 46.6 μm (90th percentile), with median of 32.8 μm. To optimize the properties of the fabricated parts, an advanced processing strategy was implemented, employing specific process parameters for the core region, a 2 mm-thick skin, and the outer contour, which was scanned twice with overlapping exposures to reduce surface roughness (see Table 4).

After the LPBF process, the specimens were removed from the build platform, heat treated at 240°C for six hours to relieve residual stresses, and machined on the outer surfaces to meet testing tolerances.

Also in this case, the lack of optical accessibility inside the Aluminium test specimen prevented direct inspection for geometric and surface characterization. Therefore, sectioned specimens consisting of a flat wall and a pair of BCC half-cells per configuration were concurrently produced for this purpose. Overall, the procedures and methods applied in this work are consistent with those adopted in previous studies [22,24], which can therefore be used for comparison.

Table 3
Chemical composition of the AlSi10Mg powders.

Chemical element	Al	Si	Mg	Fe	Ti	Zn
Content [wt%]	Base	10.38	0.26	0.17	0.02	0.01

Table 4
LPBF parameters adopted to produce the samples.

	Core surface	Skin surface	Contour I pass	Contour II pass
Power	370 W	200 W	200 W	200 W
Scanning speed	1400 mm/s	800 mm/s	1250 mm/s	350 mm/s
Spot diameter	190 μm	140 μm	100 μm	50 μm
Layer thickness	50 μm	25 μm	25 μm	25 μm
Hatch distance	0.112 mm	0.112 mm	–	–
Exposure	Checkerboard	–	–	–

2.2. Samples characterization

The geometric features of the BCC cells were examined using a Hexagon RS6 laser scanner mounted on an absolute arm featuring seven degrees of freedom. The blue light scanner captured 4,000 points at a time over 150 mm scan lines with an accuracy of 0.026 mm (2σ), while the overall measurement system accuracy was ±0.047 mm [32]. The acquired data were then post-processed to exclude points with an incidence angle exceeding 75°, reduce noise through a medium-intensity statistical filter, and maintain a minimum inter-point spacing of 0.05 mm. Subsequently, the point cloud was aligned with the CAD models through a best-fit algorithm, and deviations between measured points and nominal surfaces were calculated.

The results summarized in Tab. 5 show that the absolute mean deviation and dispersion were consistent with the process-specific accuracy across all configurations and well aligned with the outcomes of previous works [22,24]. In more detail, the mean absolute error for identical configurations differed by only 0.011 mm, while it did not exceed 0.032 mm across all configurations tested, with an overall standard deviation of $\sigma = 0.012$ mm, which reflects a satisfactory degree of manufacturing repeatability. Conversely, the maximum deviation was notably higher than previously reported, both when comparing different geometries and sizes, and within specimens of the same type [24].

In the A-BCC configuration, the maximum deviation occurred near the midpoint of the upper trusses (see Fig. 3), where a distinct discontinuity likely resulted from abrupt truss displacements caused by the progressive accumulation of thermal stresses and subsequent misalignment of layers. This phenomenon was not previously observed and highlights potential limitations in process repeatability. In particular, the build platform composition appears critical, as a high part count per build job extends cooling intervals between scans of successive layers on the same part, potentially exacerbating thermal stresses.

In the B-BCC configuration, the maximum deviation was instead found on the down-skin surfaces of the trusses, where pronounced imperfections were evident. These defects likely resulted from deformation and dross formation due to heat penetration from the solid substrate into the underlying powder bed, which in this configuration is heightened by the steep inclination angles of the surfaces. Overall, the B-BCC configuration shows inferior geometric accuracy, but it remains suitable for industrial applications.

The surface characteristics of the samples were instead analyzed using a Sensofar S neox Five Axis confocal microscope equipped with a

Table 5
Geometrical deviation of samples measured by laser-scanning.

Sample	Absolute mean deviation	Dispersion (Standard deviation)	Maximum deviation
A-BCC	0.037 mm	0.068 mm	0.422 mm
B-BCC	0.058 mm	0.094 mm	0.424 mm

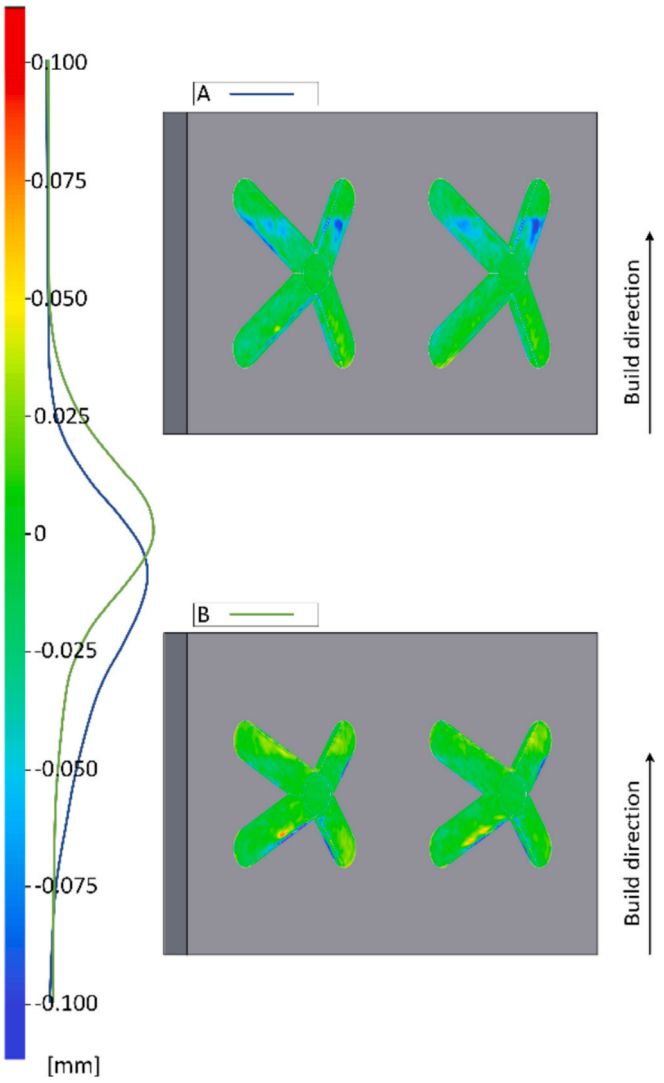

Fig. 3. Dimensional error of the A-BCC and B-BCC configurations determined by examining the sectioned samples with the laser scanner.

Nikon EPI 5x objective by scanning both the flat surface and the overlying trusses parallel to the imaging plane, with step increments of 12 μm. The green light scanner captured images at a resolution of 1224 × 1024 pixels over areas measuring 3378.24 × 2826.24 μm^2, with a 30 % overlap to enable focal plane reconstruction. Measurement accuracy and repeatability exceeded 600 nm and 20 nm, respectively [33]. The acquired data were subsequently post-processed using a dedicated low-intensity filter to reduce noise. Surface morphology was then assessed by extracting a 1 × 1 mm^2 region, which was levelled using a linear areal Gaussian filter ($\lambda_{c,FALG} = 1.144$ mm) [24].

The analysis revealed that the flat walls were smooth and devoid of significant defects, whereas the trusses were characterized by surface irregularities in the form of discrete protrusions and dips (see Fig. 4). In the A-BCC configuration, low-frequency undulations presumably induced by thermal shrinkage and stresses were also noticeable primarily on the up-skins, while they were likely masked by dross accumulation on the down-skins. Conversely, undulations were significantly attenuated in the B-BCC configuration, possibly due to the reduced slenderness of the trusses, which may limit micro-displacements during the manufacturing process. Compared to previous investigations, the truss surfaces exhibited slightly improved uniformity, with fewer localized defects on the up-skins and reduced low-frequency undulations on the down-skins.

On the other hand, the Roughness average (*Ra*) and Waviness average (*Wa*) were evaluated by extracting 4.8 mm long profiles from the centreline of the flat walls and from each truss, which were processed following the ISO 4287 standard [34], using a cut-off wavelength of $\lambda_c = 0.8$mm. This approach yielded representative roughness and waviness values that reflect intermediate surface conditions between the extremes found at the steepest overhang angles. The results presented in Table 6 show that the cell type does not have a statistically significant effect on either *Ra* ($p = 0.99$) or *Wa* ($p = 0.20$), whereas surface orientation significantly influences both parameters ($p \leq 0.05$). In more detail, *Ra* was found to be 36 % higher on the down-skins, where the accumulation of weakly sintered dross is more pronounced, while *Wa* was 85 % higher on the up-skins, where interlayer misalignments caused by thermal stresses are more pronounced. Notably, the flat walls exhibited the highest roughness and the lowest waviness.

Compared to previous investigations, the flat walls exhibited a 125 % increase in surface roughness, while waviness remained comparable. Conversely, trusses with identical geometry exhibited average increases of 87 % in roughness and 43 % in waviness, reflecting significant differences likely caused by the powder quality and aging [35], as well as the composition and nesting density of parts on the build platform.

Overall, considering all the configurations investigated in this and previous studies, the standard deviation of surface roughness for the up-skins and down-skins was found to be $\sigma_{Ra\_up} = 1.48\,\mu m$ e $\sigma_{Ra\_down} = 2.40\,\mu m$, respectively, while for surface waviness it was $\sigma_{Wa\_up} = 6.00\,\mu m$ e $\sigma_{Wa\_down} = 1.92\mu m$, respectively. These values correspond to approximately 23 % of the respective measurements in the present study, highlighting a consistent and reliable degree of manufacturing repeatability.

Finally, previous tests conducted in [36] on samples produced by the authors of the present paper using the same equipment, process parameters, and procedures showed that the thermal conductivity and thermal diffusivity of the LPBF material are $k = 175 W/(m\,K)$ and $\alpha = 73.8\,mm^2/s$, respectively.

3. Experimental apparatus and data reduction

3.1. Test facility

The test rig used to perform the experiment (Fig. 5) is installed in the Environmental and Energy Systems Laboratory at the University of Udine and is the same setup employed in the previous contributions [22,24]. Accordingly, only the main features are described here, and the reader is referred to the cited literature for further details.

The test rig is operated in suction mode by means of a centrifugal fan, whose rotational speed can be adjusted to regulate the flow rate. Ambient air is sucked into the rig through a 9:1 contraction and then flows through the smooth entry channel, which shares the same internal cross-sectional dimensions as the test specimens (i.e., 140 × 10 mm^2) and has a length equal to 155 hydraulic diameters. Then, the test specimen follows, and a second smooth channel connects its outlet to a settling chamber. Wooden flanges are used to connect the test section to both the inlet and outlet channels, serving also as thermal breaks. Finally, the air goes through two different flow meters, namely a digital YEWFLO DY025-S2 (0–100 kg/min range and ±1.0 % uncertainty), and a calibrated orifice flow meter. The digital flow meter enables for more accurate measurements at low Reynolds number (below 10000), while the orifice one is used for higher flow rates to limit the rig pressure losses and allows reaching a maximum Reynolds number of about 28000, depending on the actual geometry under test.

Pressure taps are located both upstream and downstream of the test specimen and are embedded within the connection flanges (see Fig. 5). Inlet air temperature is provided by 2 K-type thermocouples installed in the last portion of the entry channel (T_{IN} in Figs. 5 and 6), while outlet temperature is measured by 4 K-type thermocouples mounted in the

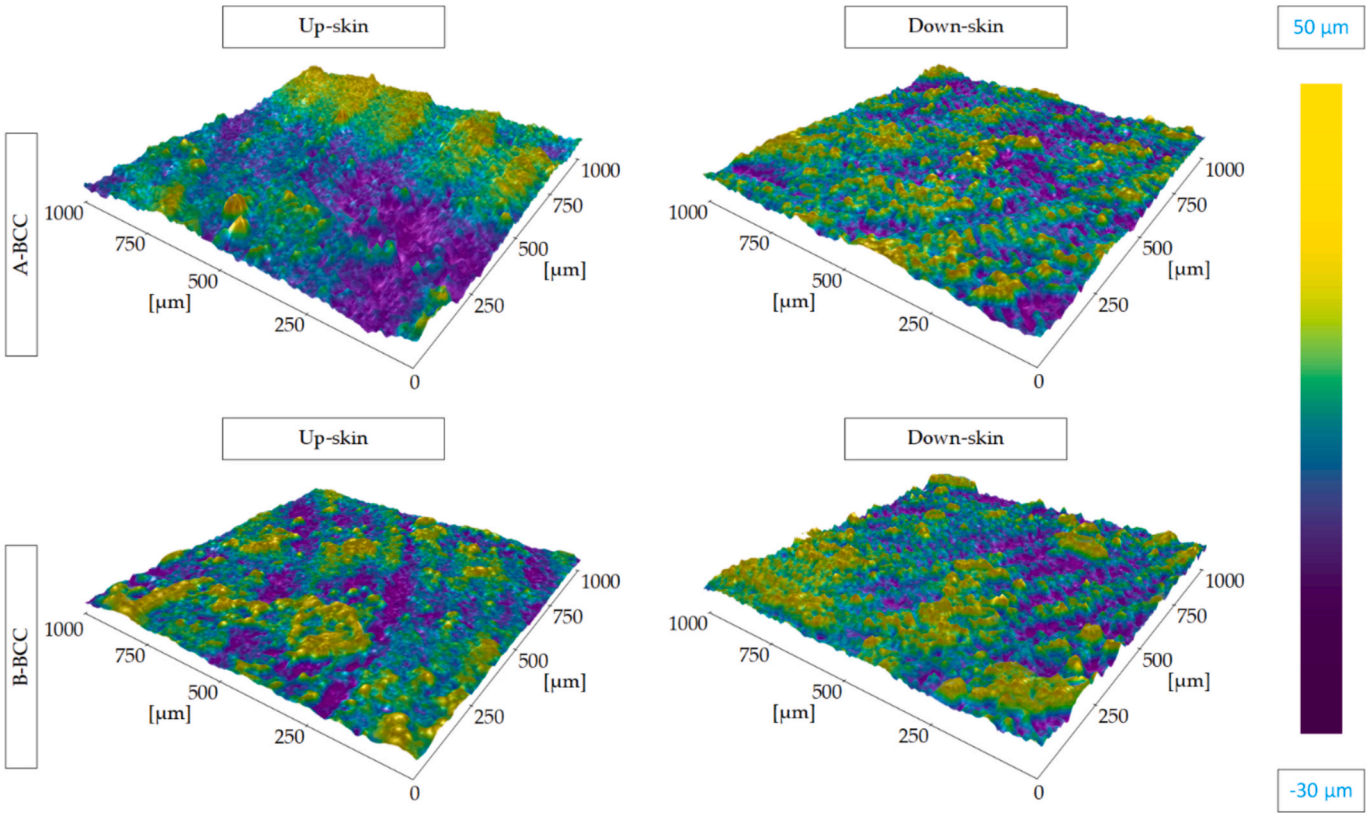

Fig. 4. Surface morphology of the up-skin and down-skin surfaces of the A-BCC and B-BCC configurations determined by examining the sectioned samples with the confocal microscope.

Table 6
Roughness average *Ra* and Waviness average *Wa* of the samples.

	$Ra(\lambda_c = 0.8$ mm) [µm]		$Wa(\lambda_c = 0.8$ mm) [µm]	
	Mean	Standard deviation	Mean	Standard deviation
Flat walls	10.63	0.37	2.95	0.01
A-BCC up-skins	7.29	0.03	25.40	2.85
A-BCC down-skins	9.00	2.26	12.15	4.73
B-BCC up-skins	6.51	0.07	17.55	5.23
B-BCC down-skins	9.82	1.86	11.04	3.37

throat section of a 5:1 contraction at the outlet of the test specimen, ($T_{OUT,c}$ in Figs. 5 and 6). This arrangement provides a better estimation of the bulk flow temperature. However, due to the very high velocities in the contraction, the thermocouple readings must be corrected for convective effects using an experimentally determined recovery factor (see [22,24] for more details). These signals are further elaborated to compute the actual temperature at the test section outlet (T_{OUT} in Fig. 6), as it will be clarified in the next section.

The heat transfer performances are measured with the assumption of constant heat flux applied to the external surfaces of the heat exchangers. This is done by adopting the hardware schematically depicted in Fig. 6, which is composed by the following components, from the test section outwards:

- An aluminium block instrumented with 12T-Type thermocouples is in contact with the external surface of the test section (high-thermal-conductivity grease, k = 11 W/m K, is applied at the interfaces)
- A thin paper sheet (resistant up to 220 *C) is used as electrical insulator
- 25 µm thick Inconel 665 alloy foil provides the required heat flux by Joule effect (powered by a variable DC supply)
- A thermal insulator foil is interposed between the Inconel foil and a MDF panel, which serves both as a support for applying compression via multiple screw jacks and as additional thermal insulation.

This stack is mirrored on both sides of the test section, with the two Inconel foils connected in series to the power supply to ensure a uniform heat flux on both external surfaces of the heat exchanger. The instrumented aluminium block, thanks to the high thermal conductivity, ensures a better uniformity of the heat supply to the test specimen. Finally, in order to reduce as much as possible the thermal dissipation towards the environment, the test section was isolated by a thick layer of rock wool.

To ensure the lowest possible experimental uncertainty, all the above mentioned thermocouples were connected to a common reference cold joint and were calibrated in a thermal oil bath (so minimizing the relative errors).

Pressure drop measurements were carried out with the test section in isothermal condition with the ambient air (i.e. without applied heat flux), to eliminate the influence of temperature-dependent fluid property variations. A water column micromanometer (0–200 mmH2O range and ±0.035 mmH2O uncertainty) was used to collect the static pressure drops across the heat exchangers.

Heat transfer measurements were carried out under stationary thermal conditions, defined as the point at which temperature readings from the aluminium blocks varied by no more than ±0.05 °C over a time interval of 15 min. At steady state, data logging started for 5 min at a sampling frequency of 1 Hz. The recorded data were then time-averaged and used to evaluate heat transfer performance, as described in the following section.

It is important to note that both the test rig and experimental methodology (including the data reduction procedures described in the next subsection) were previously validated by comparing the aerothermal performance of a smooth channel with benchmark data from

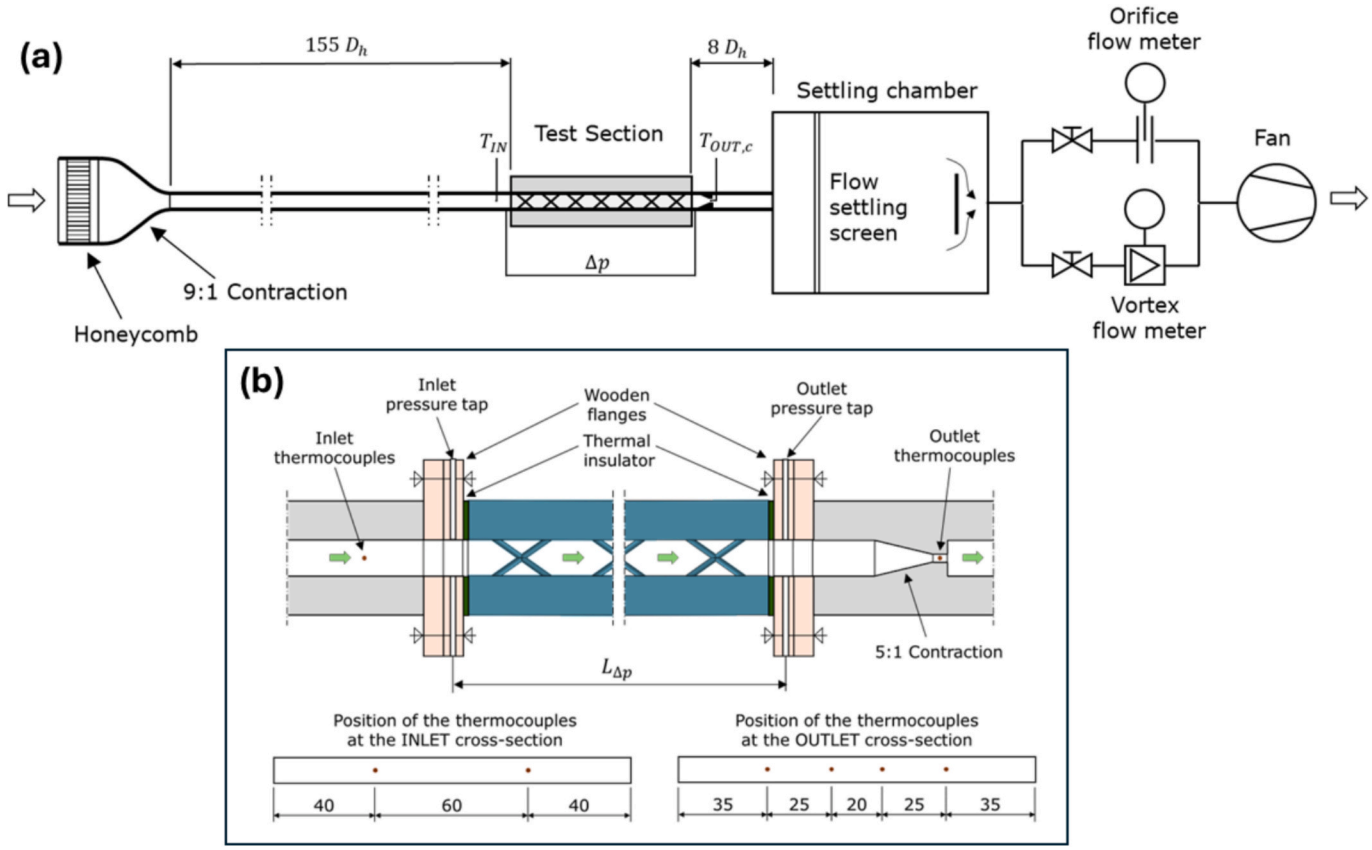

Fig. 5. Test rig layout (a) and details of the test section installation (b).

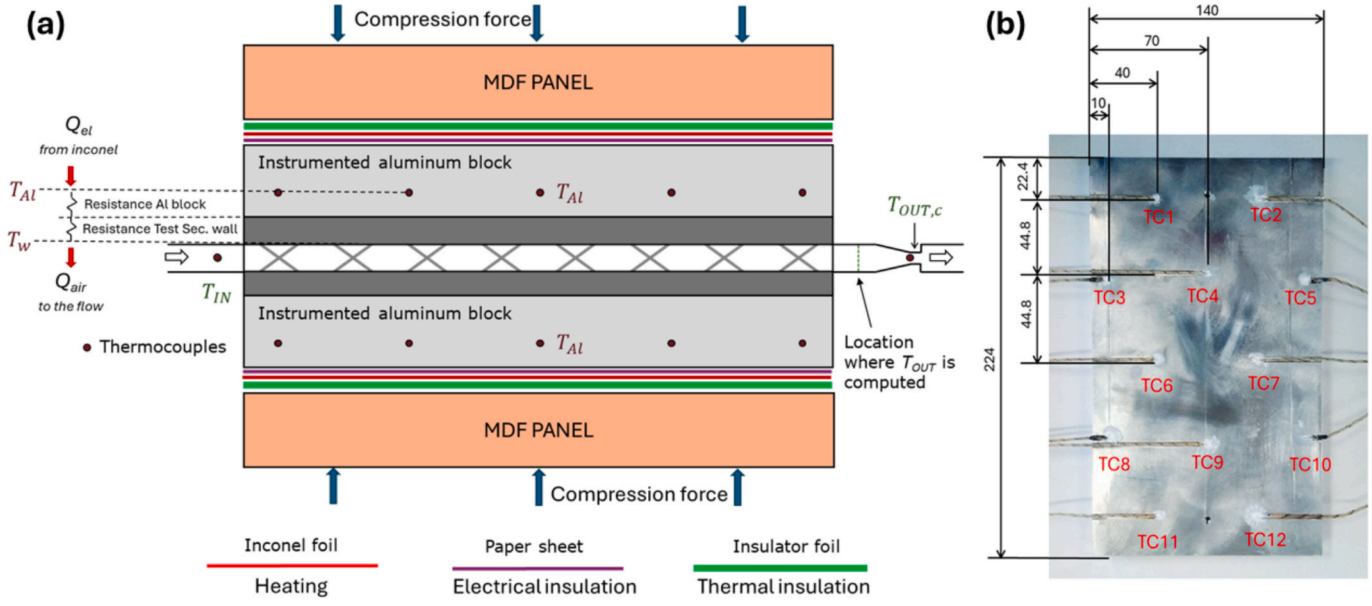

Fig. 6. Schematic view (cross section) of the test section installed for the heat transfer measurements (a), and details of the 12 thermocouples used to monitor the aluminium wall temperature (b).

the literature [22,24]. therefore, these aspects are not addressed here for the sake of brevity.

3.2. Data reduction

The aero-thermal performances of the different heat exchangers is presented in non-dimensional form by the friction factor (f) and the Nusselt number (Nu) as a function of the Reynolds number (Eq. (1)). This latter is referred to the flow condition at the test section entry and the hydraulic diameter in Eq. (2) is used as reference length scale.

$$Re = \frac{\rho U_b D_h}{\mu} \tag{1}$$

$$D_h = \frac{4A_c}{P} \tag{2}$$

where all the variables are evaluated at the inlet of the test section. In particular the values of $A_c = 140*10\text{mm}^2$ and $P = 2*(140+10)\text{mm}$ are used for all geometries, except for the modified configurations AS-mod, BS-mod, and BPS-mod, where $A_c = 125*10\text{mm}^2$ and $P = 2*(125+10)\text{mm}$ are used.

The flow resistance is quantified by the friction factor (f) defined in Eq. (3). In this equation, the static pressure difference (Δp) between upstream and downstream pressure taps accurately represents the total pressure drop. This is because of the equal size of inlet and outlet sections and the isothermal condition in which pressure drop tests were performed.

$$f = \Delta p \frac{D_h}{L_{\Delta p}} \frac{2}{\rho U_b^2} \tag{3}$$

In Eq. (3), $L_{\Delta p}$ represents the distance between the pressure taps (see Fig. 5), and both air density and bulk velocity are evaluated at the inlet of the test section.

The Nusselt number is evaluated according to Eq. (4) and attributed to the reference area $A_r = 140*224\text{mm}^2$ (i.e. the surface of the confining plates, see Fig. 2). The reference area is reduced to the smaller value of $A_r = 125*224\text{mm}^2$ for the modified geometries AS-mod, BS-mod, and BPS-mod.

$$Nu = h\frac{D_h}{k} = \frac{Q_{el}}{A_r \Delta T_{ml}} \frac{D_h}{k} \tag{4}$$

The input power Q_{el} to compute the Nusselt number is assumed equal to the electric DC power supplied to the Inconel sheets:

$$Q_{el} = EI \tag{5}$$

It has to be mentioned that not all the input electric power is dissipated by the air flow convection. A portion is inevitably lost through conduction in the test rig and to the surrounding environment. However, thanks to the good thermal insulation of the test section, the heat losses were limited to few percent of the input value, as can be appreciated in Fig. 7 where the power balance computed according to Eq. (6) is reported.

$$Q_{air} = \dot{m} c_p \left(T_{OUT,c} - T_{IN}\right) + \dot{m}\frac{U_{OUT,c}^2 - U_{IN}^2}{2} \tag{6}$$

For most tests, the power balance remained within ±5 %, which is sufficiently low to avoid additional effort for the estimation of power losses.

As the temperature difference for computing the Nu number, the logarithmic mean value is chosen and computed according to Eq. (7).

$$\Delta T_{ml} = \frac{T_{OUT} - T_{IN}}{\ln\left(\frac{T_{OUT} - T_w}{T_{IN} - T_w}\right)} \tag{7}$$

In this equation, T_{IN} is the flow inlet temperature, computed as the averaged value of the inlet thermocouples readings (Fig. 5). T_{OUT} comes from the averaged values of 4 temperature measurements at the outlet throat section ($T_{OUT,c}$ in Figs. 5 and 6) and assuming a flow evolution at constant total enthalpy from test section outlet and throat sections [24]. Finally, the aluminium internal wall temperature T_w is computed from the temperature readings of the of the thermocouples inside the instrumented aluminium blocks and by means of a 1D conduction analysis as described in Eq. (8).

$$T_w = T_{Al} - RQ_{el} \tag{8}$$

The overall thermal resistance ($R = 9.39\ 10^{-5}\ \text{m}^2\text{K/W}$) is estimated by a series of resistances, as depicted in Fig. 6. The thermal conductivity of the test specimens was available from experimental measurements, while that of the aluminium blocks was derived from the vendor's datasheet. Since thermally conductive paste was applied during the assembly of the heating elements, and the components were firmly pressed against the test section, the contact thermal resistance was neglected in the calculation (the thermal contact resistance at the interface, filled with the conductive grease, is estimated about 35 time lower than that of metal parts).

T_{Al} in Eq. (8) represents the average of the readings from the 12 thermocouples embedded in each aluminium block. It was decided to use the average values since the experimental data show a very limited variation of the metal temperature among the different positions (typically, the spatial variation was ±1.15 °C about the averaged value).

To estimate the experimental uncertainty associated with the performance parameters, the same approach adopted in [22] and based on the Kline and McClintock's method [37] was used. Consequently, only some of the estimates are here reported. At Reynolds number below 7500, upper estimates of about 11.3 % and 9.1 % can be assumed for the uncertainties about the friction factor and Nusselt number, respectively. At higher Reynolds numbers (above about 8000), the uncertainty drops down to a maximum of 5.2 % for the friction factor and 6.3 % for the

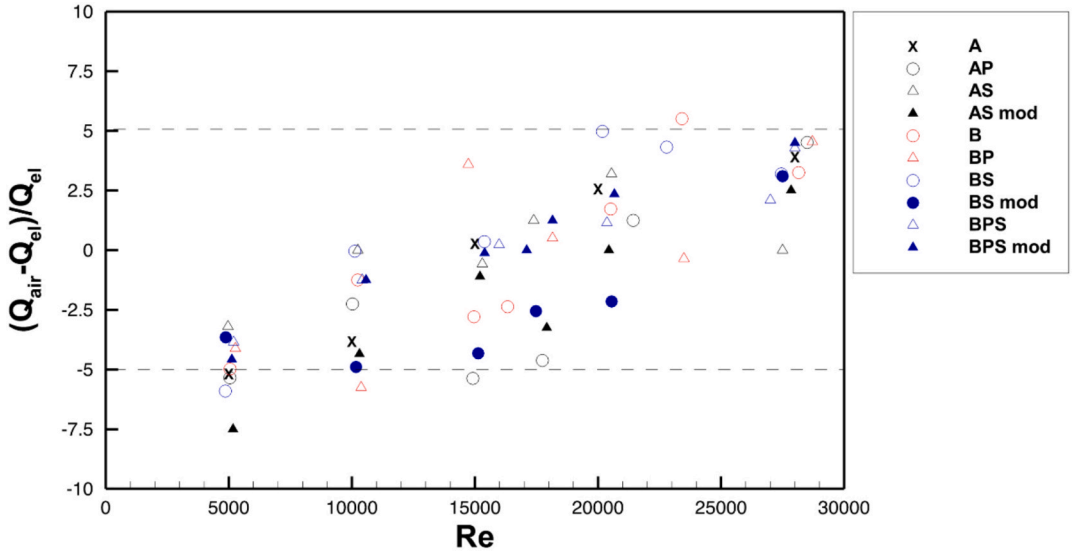

Fig. 7. Power balance as a function of the Reynolds number.

Nusselt number. For the Reynolds number, the uncertainty estimate is below 3.8 % in the whole range here investigated. Experimental repeatability was also assessed at the lowest and highest flow conditions (Re = 5000 and Re = 27000) through six repeated tests for geometries AS, AP, B, BS, and BP, yielding a repeatability within 7.5 %.

4. Results and discussion

4.1. Results for A geometry

Fig. 8 reports the friction factor and the Nusselt number for the starting geometry A and those derived therefrom. Although geometry A was already investigated in [24], it was tested again in this experimental campaign to provide a baseline and to verify the proper functioning of the test rig, successfully confirming previous results. By comparing the data of A and AP geometries, the effect of a pitch reduction can be appreciated: it determines an increase of pressure losses associated with an increase of Nusselt number. The friction factor for AP is approximately 6 % higher than that of A across all tested flow regimes, as expected given that the pitch reduction involves the introduction of an extra row of BCC. This also translates in a higher heat transfer capability that is more pronounced for Re above 15000.

In contrast, changing the matrix arrangement reduces the total number of BCC cells and increases the spacing between the first and last cell in a row and the lateral confining walls (compare geometries A and AS in Fig. 1). As a result, the friction factor for AS is approximately 32 % lower than that of A, and this is accompanied by a significant reduction in thermal performance, with the Nusselt number decreasing by about 15 %. Obviously, there is a doubt that this drastic decrease in pressure losses and heat exchange capacities is associated with the possible lateral bypass flow that could arise given the new arrangement of the cells on the matrix. However, this doubt can be resolved by comparing the data for AS and AS-mod. In the latter configuration, the minimum distance between the BCC and the lateral wall is equal to that of geometry A (with a consequent reduction of the D_h, see Fig. 1 and Table 2). The friction factor and Nusselt number for AS-mod are only marginally higher than those of AS, confirming that although some bypass flow occurs, its impact on overall performance is limited. It is therefore possible to conclude that the difference in performance with respect to configuration A is mainly due to the matrix arrangement.

4.2. Results for B geometry

Geometry B introduces a modification to the BCC truss inclination angle (Fig. 2), altering the shape of the unit cell. Surprisingly, this has practically no effects on the aero-thermal performance, as can be appreciated in Fig. 9. Friction losses and Nu number are nearly identical for geometries A and B, which are the same in all respects except for the truss inclination. The same observation holds when comparing geometries AS and BS. It can be therefore concluded that the inclination of the BCC truss (which modifies the footprint of the elementary cell) does not significantly affect the internal fluid dynamics (which govern the forced convection process) or the conjugate conduction within the metal.

The effects of the variation of the other geometrical parameters on the aero-thermal performances of geometry type B are reported in Fig. 10. A reduction of the streamwise pitch produces also in this case an increase of both pressure losses and heat transfer (compare B vs BP and BS vs BPS) but, differently from geometry A, the differences are more pronounced. Indeed, for both B and BS geometries, the pitch reduction determines the addition of three more rows of BCC (see Fig. 1) which turns into higher augmentation of the friction factor (about 18 % more) and Nu (about 15 % more). In contrast, the pitch reduction in geometry A accommodates only one additional row, resulting in a less pronounced variation in performance (see previous subsection and Fig. 8).

Staggering the BCC rows by half a crosswise pitch in geometry B yields similar effects to those observed in geometry A (Fig. 10, compare B vs BS and BP vs BPS): the friction factor decreases significantly (approximately 21 %) but this is unfortunately coupled with an equally significant decrease in heat transfer (approximately 15 %).

Also in this case, −mod geometries were tested for BS and BPS, showing no remarkable effects of a possible lateral bypass flow.

Overall, among the B-type geometries, and with respect to the starting A geometry which gives identical results to B geometry, the best performant in terms of heat transfer is geometry BP (with reduced pitch) but at the cost of higher pressure losses. On the contrary, the combination of reduced pitch and rows arrangement staggered of half a crosswise pitch (BPS geometry) allows attaining equal heat transfer as the starting geometry but with superior performance in terms of friction factor.

It is clear that the results commented above are, to some extent, affected by the change of the number of unitary cells and rows among the different specimens. Therefore, an attempt was made to find a reference length for a new performance data normalisation that could scale these effects. Since the actual experimental campaign considers

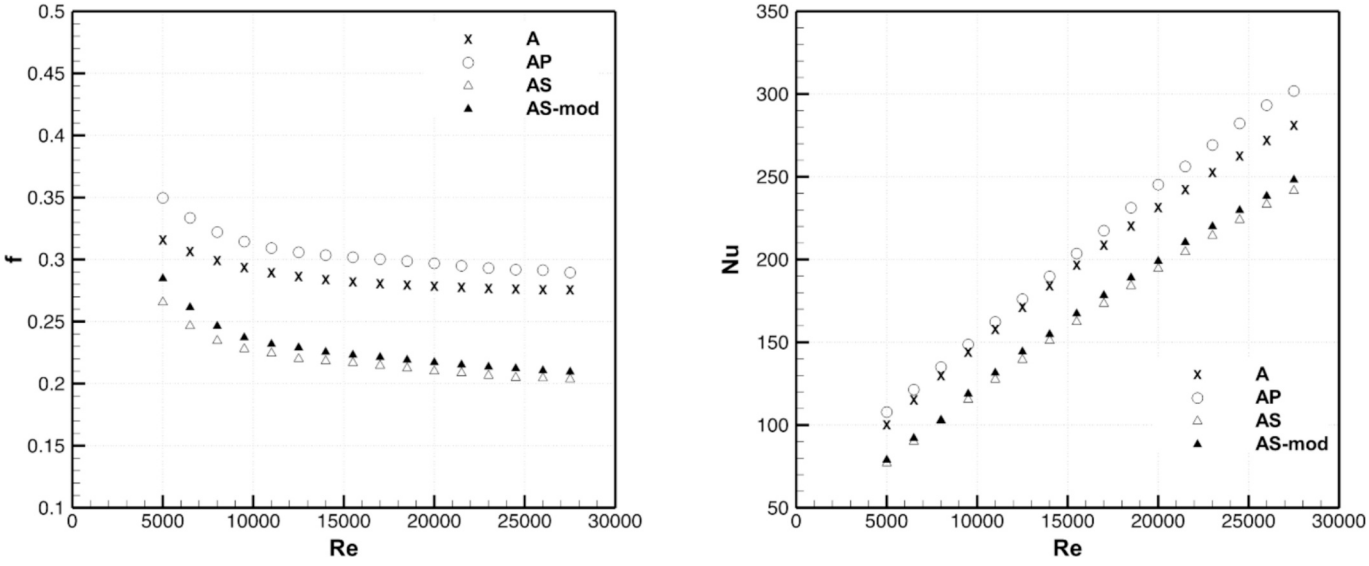

Fig. 8. Friction factor and Nusselt number as function of the Reynolds number for type A geometries.

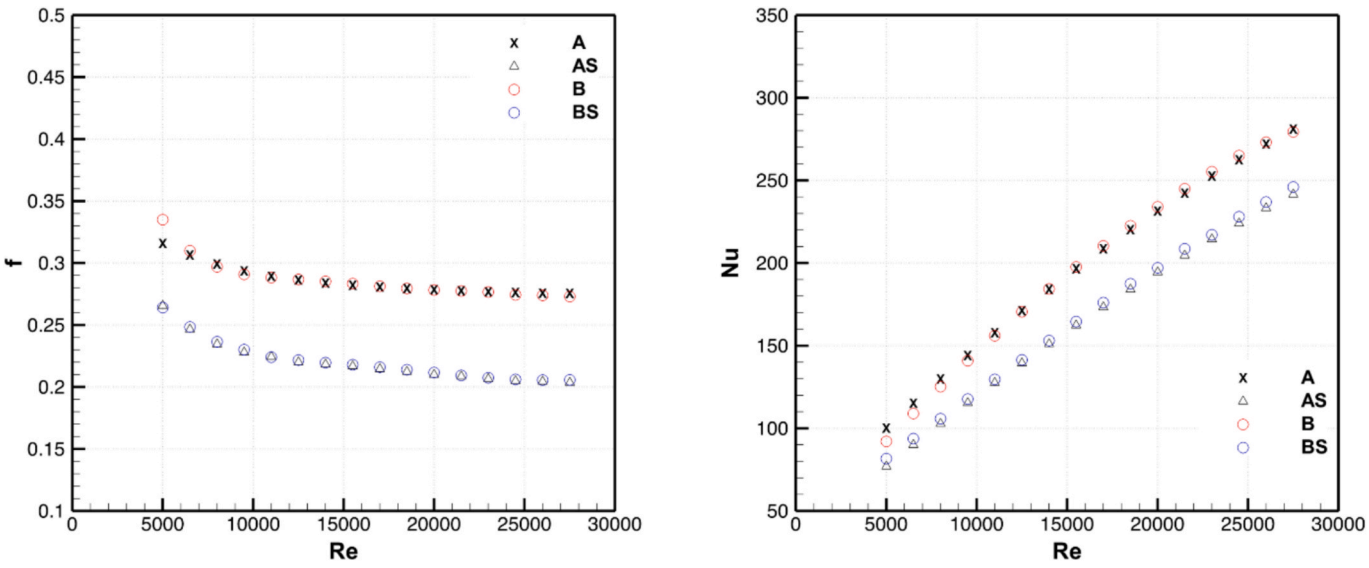

Fig. 9. Effects of the BCC shape on the aero-thermal performances.

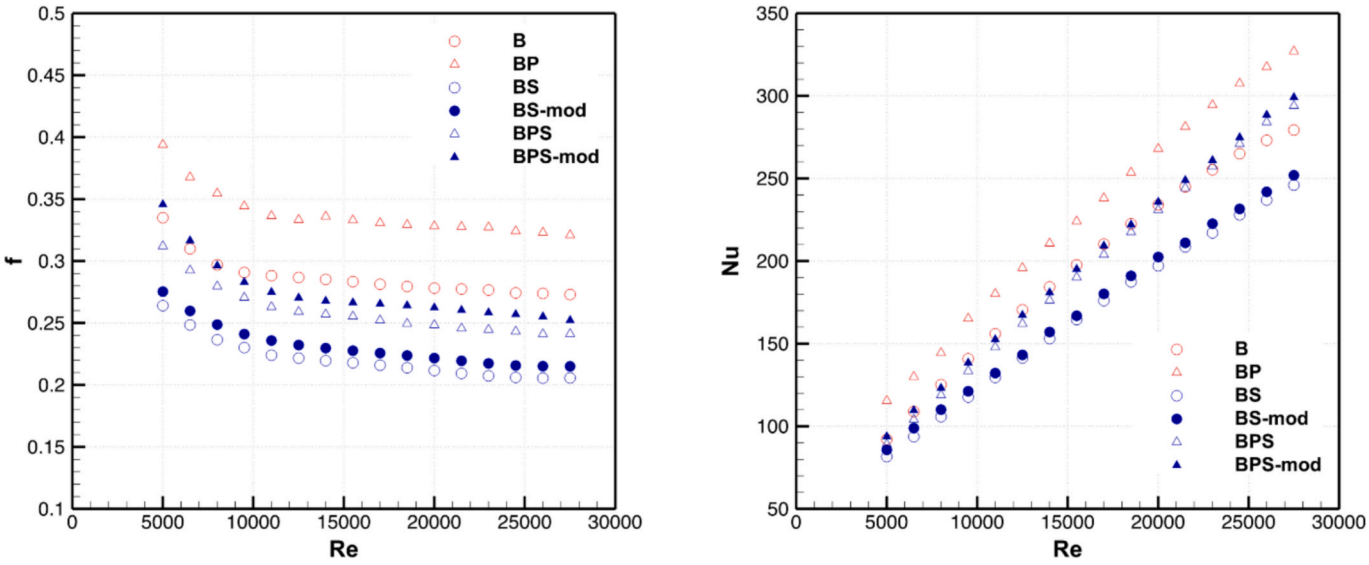

Fig. 10. Friction factor and Nusselt number as function of the Reynolds number for type B geometries.

specimens of equal external dimensions, the number of rows can be represented by the streamwise pitch value, S_x. The number of elements determines the "porosity" of the heat exchanger, a characteristic that can be well expressed by the heat exchanger hydraulic diameter defined in Eq. (9):

$$D_{BCC} = \frac{4\int_0^L A_c(l)dl}{A_w} = \frac{4V_w}{A_w} \tag{9}$$

where V_w is the enclosed wetted volume and A_w is the total wetted surface area. This definition of hydraulic diameter is commonly used in channels with non-uniform cross-section areas in the flow direction [38], as in the present case. An increase in the number of BCC cells leads to a greater wetted surface and a reduced enclosed volume, thereby decreasing the value of D_{BCC}.

Therefore, the Nusselt number and the friction factor definitions were modified by introducing the ratio between S_x and D_{BCC}, and the best fit was found to follow a power law rather than a linear dependence, as in Eqs. (10) and (11).

$$f_n = \Delta p \frac{D_h}{L_{\Delta p}} \frac{2}{\rho U_b^2} \left(\frac{S_x}{D_{BCC}}\right)^{0.69} = f\left(\frac{S_x}{D_{BCC}}\right)^{0.69} \tag{10}$$

$$Nu_n = h\frac{D_h}{k}\left(\frac{S_x}{D_{BCC}}\right)^{0.69} = Nu\left(\frac{S_x}{D_{BCC}}\right)^{0.69} \tag{11}$$

Fig. 11 shows the performance data after applying the proposed normalization for those geometries that differ only in the number of rows and unit cells (i.e., pairs A/AP, B/BP, and BS/BPS), demonstrating that the method effectively collapses the data onto unified trends. Performance data of A and AP collapse on the same curve and the same happens for the B geometries. It has to be observed that very different variations of pitch (or number of rows) can be taken into account. Indeed, for A geometries the pitch varies from 28 mm to 24 mm (or from 8 to 9 BCC rows), while for the B type geometries the initial pitch of 28 mm is lowered down to 20 mm (or from 8 to 11 BCC rows).

It is clear that the proposed normalization works for the present data and, most likely, a better fitting could be found if a wider data base could be available. However, the evidence that the correlation works on two

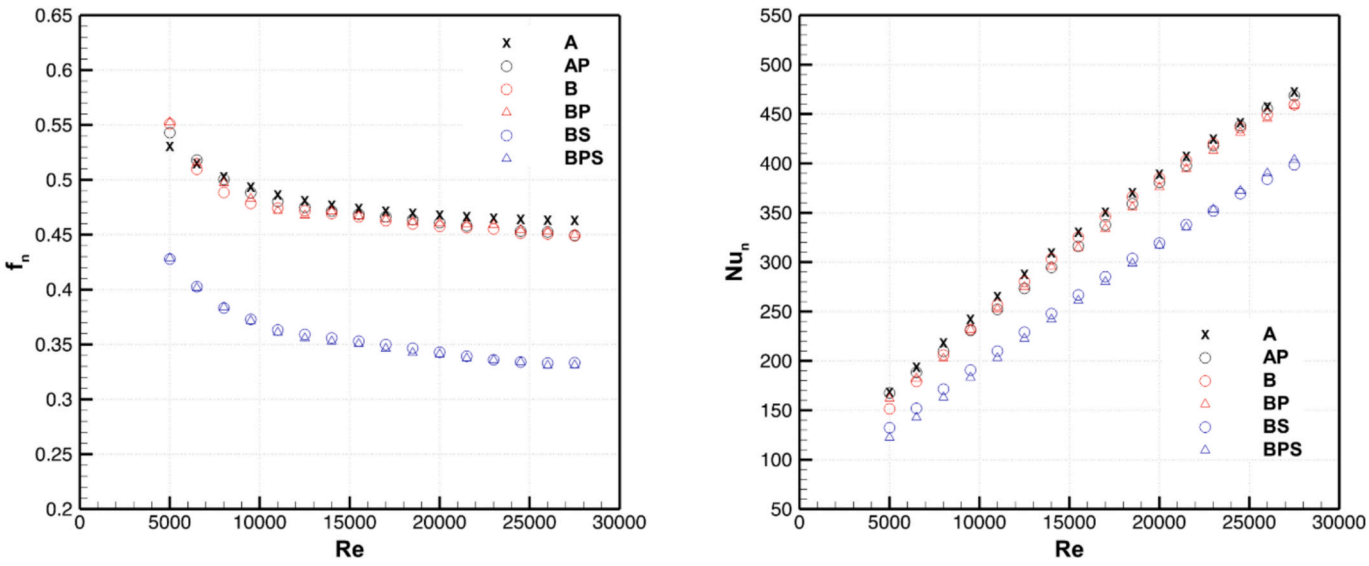

Fig. 11. Modified friction factor (fn) and modified Nusselt number (Nun): comparison for geometries of different streamwise pitch and number of BCC elements.

different types of matrix arrangements and that the power exponent is the same for both Nu and friction factor, are clear indications of its physical soundness and, most likely, of its general validity for BCC types of lattice structures.

To better appreciate and evaluate the trade-off between pressure loss and heat transfer augmentation, the TPF firstly introduced by [39] can be used. It is defined as in Eq, (10), and it compares the efficiency index ($Nu/f^{1/3}$) of a given geometry with respect to the same index but for the smooth channel and at the same Reynolds number:

$$TPF = \frac{Nu/f^{1/3}}{Nu_0/f_0^{1/3}} \tag{12}$$

Smooth channel values are obtained from well-known literature correlations: the Colebrook correlation for the friction factor [40], and the Gnielinski correlation [41] for the Nusselt number. The TPF values for all the heat exchangers tested in this study are given in Fig. 12. For the sake of clarity, the data for the −mod versions are not provided as they offer no substantial performance difference compared to their corresponding base geometries, as discussed above.

For A-type geometries, reducing the pitch (geometry AP) leads to a modest TPF increase only at Reynolds numbers above 20000, while the alternative row arrangement (AS) consistently shows lower performance across the entire investigated range. This same observation holds true for B-type geometries. The BCC shape modification alone does not significantly improve TPF unless combined with pitch reduction, geometry BP is the best performer overall.

5. Conclusions

This paper investigated the influence of cell geometry, spatial configuration, and streamwise pitch on the thermal and hydraulic performance of aluminium heat exchangers incorporating BCC structures manufactured via LPBF.

The preliminary characterization showed that the geometrical conformity of the investigated structures was on average consistent with the process-specific accuracy across all configurations, although non-negligible defects caused by thermal stresses and dross formation locally impacted part quality. The cell type had no statistically significant effect on *Ra* or *Wa*, which were typically higher on the up-skins and

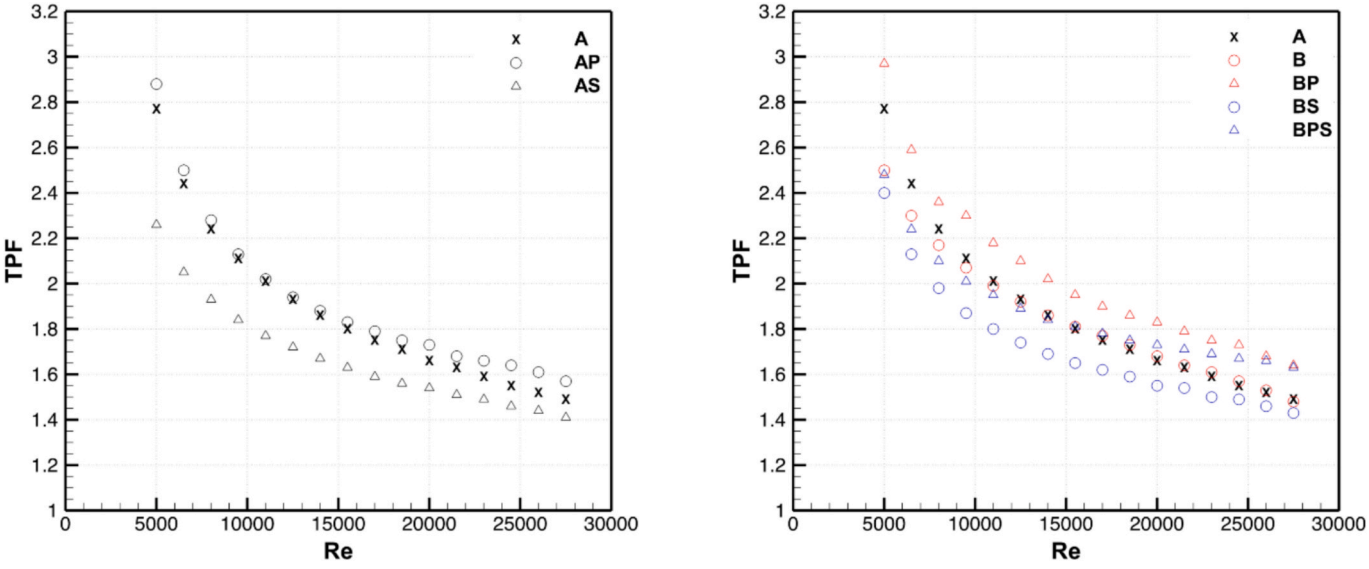

Fig. 12. Thermal performance factor comparison.

down-skins, respectively, suggesting that thermal stresses and dross formation are again the dominant factors. Notably, flat walls exhibited the highest *Ra*, highlighting the importance of optimising this feature to minimise pressure losses.

From the experimental campaign, several key findings emerged:

- Reducing the pitch consistently increased both pressure losses and heat transfer, with the effect being more pronounced in geometries with smaller unit cell footprints (type B), where a greater number of elements could be added.
- Staggered cell arrangements reduced both pressure drop and thermal performance, suggesting a less favourable interaction between flow and heat transfer surfaces.
- Changes in truss inclination had negligible impact on both the friction factor and the Nusselt number, despite modifying the unit cell footprint.

A normalization method, based on the ratio between streamwise pitch and a modified hydraulic diameter related with the porosity of each heatsink matrix, successfully collapsed data from different configurations onto unified scaling curves for both friction factor and Nusselt number, indicating that experimental correlations could be derived to estimate pressure losses and heat transfer for this specific BCC geometries.

The thermal performance factor highlighted that while reducing pitch generally improves heat transfer, it does not always yield the best trade-off with pressure losses. Among the tested geometries, BP provided the highest thermal enhancement but incurred increased pressure drop, whereas BPS offered the most balanced compromise between heat transfer and flow resistance.

In conclusion, this study demonstrates how relatively simple variations in BCC-based heat sink geometry—namely pitch, spatial arrangement, and truss inclination—can be strategically manipulated to tailor thermal and hydraulic performance. The proposed normalization approach provides a practical tool for comparative evaluation and preliminary design. Future work will aim to extend the normalization framework to include crosswise pitch variations, alternative cell orientations, and different lattice architectures, thereby enhancing prediction capabilities and supporting the development of next-generation additively manufactured heat exchangers.

CRediT authorship contribution statement

Emanuele Vaglio: Writing – review & editing, Writing – original draft, Methodology, Investigation, Data curation, Conceptualization. **Federico Scalzo:** Writing – review & editing, Writing – original draft, Methodology, Investigation, Data curation, Conceptualization. **Nicolò Scussolin:** Writing – review & editing, Writing – original draft, Investigation. **Luca Casarsa:** Writing – review & editing, Writing – original draft, Methodology, Investigation, Formal analysis, Data curation, Conceptualization.

Declaration of competing interest

The authors declare that they have no known competing financial interests or personal relationships that could have appeared to influence the work reported in this paper.

Acknowledgments

The Laboratory for Advanced Mechatronics - LAMA FVG - of the University of Udine is gratefully acknowledged. LAMA FVG is an international research centre for product and process innovation where the three Universities of Friuli Venezia Giulia Region (Italy) synergically cooperate for promoting R&D activities at academic and industrial levels. Emanuele Vaglio is grateful for funding under the REACT EU Italian PON 2014-2020 Program - Action IV.4 - Innovation (DM 1062, 10/08/2021).

Data availability

Data will be made available on request.

References

[1] F. Careri, R.H.U. Khan, C. Todd, M.M. Attallah, Additive manufacturing of heat exchangers in aerospace applications: a review, Appl. Therm. Eng. 235 (2023) 121387, https://doi.org/10.1016/J.APPLTHERMALENG.2023.121387.
[2] I. Kaur, P. Singh, State-of-the-art in heat exchanger additive manufacturing, Int. J. Heat Mass Transf. 178 (2021) 121600, https://doi.org/10.1016/J.IJHEATMASSTRANSFER.2021.121600.
[3] B.M. Nafis, R. Whitt, A.C. Iradukunda, D. Huitink, Additive manufacturing for enhancing thermal dissipation in heat sink implementation: a review, Heat Transfer Eng. 42 (2021) 967–984, https://doi.org/10.1080/01457632.2020.1766246.
[4] D. Jafari, W.W. Wits, The utilization of selective laser melting technology on heat transfer devices for thermal energy conversion applications: a review, Renew. Sustain. Energy Rev. 91 (2018) 420–442, https://doi.org/10.1016/J.RSER.2018.03.109.
[5] M. Sortino, G. Totis, F. Scalzo, E. Vaglio, Preliminary investigation of static and dynamic properties of SLM lattice structures for robotic applications, Mech. Mach. Sci. 66 (2019) 260–267, https://doi.org/10.1007/978-3-030-00365-4_31.
[6] S. Das, E. Rasouli, T. Ziev, N. Lamprinakos, J. Seo, A. Rollett, P. Vaishnav, V. Narayanan, Design and techno economic optimization of an additively manufactured compact heat exchanger for high temperature and high pressure applications, Appl. Therm. Eng. 245 (2024) 122778, https://doi.org/10.1016/J.APPLTHERMALENG.2024.122778.
[7] S. Sun, T.A. Moreira, B. Rankouhi, X. Yu, I.W. Jentz, D.J. Thoma, M.H. Anderson, X. Qian, Topology optimization, additive manufacturing and thermohydraulic testing of high-temperature heat exchangers, Int. J. Heat Mass Transf. 242 (2025) 126809, https://doi.org/10.1016/J.IJHEATMASSTRANSFER.2025.126809.
[8] A.S. Sabau, A. Bejan, D. Brownell, K. Gluesenkamp, B. Murphy, F. List, K. Carver, C. R. Schaich, J.W. Klett, Design, additive manufacturing, and performance of heat exchanger with a novel flow-path architecture, Appl. Therm. Eng. 180 (2020) 115775, https://doi.org/10.1016/J.APPLTHERMALENG.2020.115775.
[9] H. Rastan, A. Abdi, B. Hamawandi, M. Ignatowicz, J.P. Meyer, B. Palm, Heat transfer study of enhanced additively manufactured minichannel heat exchangers, Int. J. Heat Mass Transf. 161 (2020) 120271, https://doi.org/10.1016/J.IJHEATMASSTRANSFER.2020.120271.
[10] K. Yan, H. Deng, Y. Wu, T. Yu, Y. Xiao, J. Wang, Gyroid-structured heat exchanger optimization via lattice geometric manipulation for enhanced thermo-hydraulic performance: an experimental and numerical research, Int. J. Therm. Sci. 215 (2025) 109966, https://doi.org/10.1016/J.IJTHERMALSCI.2025.109966.
[11] M. Beer, R. Rybár, Optimisation of heat exchanger performance using modified gyroid-based TPMS structures, Processes 2024 (12) (2024) 2943, https://doi.org/10.3390/PR12122943.
[12] S.Y. Lee, K.W. Kim, D.H. Kim, M.S. Yang, J.W. Kim, G. Choi, J.W. Lee, I.S. Park, Optimization study on the uniform temperature of an additively manufactured cooler for a semiconductor heating device, Appl. Therm. Eng. 225 (2023) 120178, https://doi.org/10.1016/J.APPLTHERMALENG.2023.120178.
[13] N. Song, W. Pu, L. Qiao, B. Wu, R. Liu, F. Luo, Numerical simulation study on the heat transfer and flow characteristics of fuel/lubricating oil heat exchanger based on triply periodic minimal surface (TPMS), Appl. Therm. Eng. 257 (2024) 124437, https://doi.org/10.1016/J.APPLTHERMALENG.2024.124437.
[14] S. Catchpole-Smith, R.R.J. Sélo, A.W. Davis, I.A. Ashcroft, C.J. Tuck, A. Clare, Thermal conductivity of TPMS lattice structures manufactured via laser powder bed fusion, Addit. Manuf. 30 (2019) 100846, https://doi.org/10.1016/J.ADDMA.2019.100846.
[15] E. Vaglio, F. Scalzo, M. Sortino, L. Casarsa, Heat transfer and pressure loss performance of additively manufactured metamaterials in annular channels, Energies 2025 (18) (2025) 2486, https://doi.org/10.3390/EN18102486.
[16] W. Tang, J. Guo, F. Yang, L. Zeng, X. Wang, W. Liu, J. Zhang, C. Zou, L. Sun, Y. Zeng, Z. Zhang, J. Fu, Y. Zhao, Performance analysis and optimization of the Gyroid-type triply periodic minimal surface heat sink incorporated with fin structures, Appl. Therm. Eng. 255 (2024) 123950, https://doi.org/10.1016/J.APPLTHERMALENG.2024.123950.
[17] S. Gao, S. Qu, J. Ding, H. Liu, X. Song, Influence of cell size and its gradient on thermo-hydraulic characteristics of triply periodic minimal surface heat exchangers, Appl. Therm. Eng. 232 (2023) 121098, https://doi.org/10.1016/J.APPLTHERMALENG.2023.121098.
[18] J.S. Huang, C.Y. Wang, Numerical simulation and measurement of effective thermal conductivity of an additively manufactured lattice microstructure with gradient porosity, Results Eng. 25 (2025) 104177, https://doi.org/10.1016/J.RINENG.2025.104177.
[19] K. Park, B. Soo Kang, S. Kim, Influence of design parameters on natural convection heat transfer in additively manufactured body centered cubic lattice structures, Int. J. Therm. Sci. 205 (2024) 109250, https://doi.org/10.1016/J.IJTHERMALSCI.2024.109250.

[20] K.N. Son, J.A. Weibel, V. Kumaresan, S.V. Garimella, Design of multifunctional lattice-frame materials for compact heat exchangers, Int. J. Heat Mass Transf. 115 (2017) 619–629, https://doi.org/10.1016/J.IJHEATMASSTRANSFER.2017.07.073.
[21] A. Narkhede, N. Gnanasekaran, A.K. Yadav, Detailed thermo-hydraulic investigation of 3D octet lattice structure integrated heat sink, Int. Commun. Heat Mass Transfer 160 (2025) 108345, https://doi.org/10.1016/J.ICHEATMASSTRANSFER.2024.108345.
[22] A. Lorenzon, E. Vaglio, L. Casarsa, M. Sortino, Experimental investigation of heat transfer and pressure losses across staggered body centered cubic arrays fabricated by laser powder bed fusion, Appl. Therm. Eng. 227 (2023) 120381, https://doi.org/10.1016/j.applthermaleng.2023.120381.
[23] M. Wong, I. Owen, C.J. Sutcliffe, A. Puri, Convective heat transfer and pressure losses across novel heat sinks fabricated by selective laser melting, Int. J. Heat Mass Transf. 52 (2009) 281–288, https://doi.org/10.1016/J.IJHEATMASSTRANSFER.2008.06.002.
[24] A. Lorenzon, E. Vaglio, L. Casarsa, G. Totis, Effects of different cross-sections of Body Centered Cubic cells on pressure drop and heat transfer of additively manufactured heat sinks, Int. J. Heat Mass Transf. 222 (2024) 125170, https://doi.org/10.1016/j.ijheatmasstransfer.2024.125170.
[25] U. Kemerli, K. Kahveci, Conjugate forced convective heat transfer in a sandwich panel with a Kagome truss core: the effects of strut length and diameter, Appl. Therm. Eng. 167 (2020) 114794, https://doi.org/10.1016/J.APPLTHERMALENG.2019.114794.
[26] P. Narato, M. Wae-hayee, N. Kaewchoothong, C. Nuntadusit, Heat transfer enhancement and flow characteristics in a rectangular channel having inclined pin arrays mounted on the endwall surface, Int. Commun. Heat Mass Transfer 122 (2021) 105162, https://doi.org/10.1016/J.ICHEATMASSTRANSFER.2021.105162.
[27] A. Maji, D. Bhanja, P.K. Patowari, Numerical investigation on heat transfer enhancement of heat sink using perforated pin fins with inline and staggered arrangement, Appl. Therm. Eng. 125 (2017) 596–616, https://doi.org/10.1016/J.APPLTHERMALENG.2017.07.053.
[28] J. Zhao, S. Huang, L. Gong, Z. Huang, Numerical study and optimizing on micro square pin-fin heat sink for electronic cooling, Appl. Therm. Eng. 93 (2016) 1347–1359, https://doi.org/10.1016/J.APPLTHERMALENG.2015.08.105.
[29] A. Lorenzon, E. Vaglio, L. Casarsa, M. Sortino, G. Totis, G. Saragò, E. Lendormy, J. Raukola, Heat transfer and pressure loss performances for additively manufactured pin fin arrays in annular channels, Appl. Therm. Eng. 202 (2022) 117851, https://doi.org/10.1016/j.applthermaleng.2021.117851.
[30] A.A. Sertkaya, M. Ozdemir, E. Canli, Effects of pin fin height, spacing and orientation to natural convection heat transfer for inline pin fin and plate heat sinks by experimental investigation, Int. J. Heat Mass Transf. 177 (2021) 121527, https://doi.org/10.1016/J.IJHEATMASSTRANSFER.2021.121527.
[31] L. Xu, J. Li, K. Sun, L. Xi, J. Gao, Y. Li, Heat analysis and optimal design of fin-and-tube heat exchanger with X-truss vortex generators, Int. Commun. Heat Mass Transfer 152 (2024) 107248, https://doi.org/10.1016/J.ICHEATMASSTRANSFER.2024.107248.
[32] ISO 10360-8:2013 - Geometrical product specifications (GPS) — Acceptance and reverification tests for coordinate measuring systems (CMS) — Part 8: CMMs with optical distance sensors, (2013). https://www.iso.org/standard/54522.html (accessed June 9, 2025).
[33] ISO/IEC Guide 98-3:2008 - Uncertainty of measurement — Part 3: Guide to the expression of uncertainty in measurement (GUM:1995), (2008). https://www.iso.org/standard/50461.html (accessed June 9, 2025).
[34] ISO 4287:1997 - Geometrical Product Specifications (GPS) — Surface texture: Profile method — Terms, definitions and surface texture parameters, (1997). https://www.iso.org/standard/10132.html (accessed June 9, 2025).
[35] A. Lanzutti, F. Sordetti, R. Montanari, A. Varone, E. Marin, F. Andreatta, S. Maschio, E. Furlani, M. Magnan, E. Vaglio, E. Pakhomova, M. Sortino, G. Totis, L. Fedrizzi, Effect of powder recycling on inclusion content and distribution in AISI 316L produced by L-PBF technique, J. Mater. Res. Technol. 23 (2023) 3638–3650, https://doi.org/10.1016/J.JMRT.2023.02.017.
[36] A. Diani, L. Moro, L. Rossetto, Melting of Paraffin waxes embedded in a porous matrix made by additive manufacturing, Appl. Sci. 11 (2021) 5396, https://doi.org/10.3390/APP11125396.
[37] S. Kline, F. McClintock, Describing uncertainties in single-sample experiments, Mech. Eng. 75 (1953) 3–8.
[38] J.E. Hesselgreaves, R. Law, D. Reay, Compact heat exchangers : selection, design and operation, Butterworth-Heinemann, 2016.
[39] R.L. Webb, E.R.G. Eckert, Application of rough surfaces to heat exchanger design, Int. J. Heat Mass Transf. 15 (1972) 1647–1658, https://doi.org/10.1016/0017-9310(72)90095-6.
[40] C.F. Colebrook, C.M. White, Experiments with fluid friction in roughened pipes, Proc. R. Soc. Lond. A Math. Phys. Sci. 161 (1937) 367–381, https://doi.org/10.1098/RSPA.1937.0150.
[41] V. Gnielinski, New equations for heat and mass transfer in the turbulent flow in pipes and channels, NASA STI/Recon Technical Report A 41 (1975) 8–16. https://ui.adsabs.harvard.edu/abs/1975STIA...7522028G/abstract (accessed June 9, 2025).